

Article

# Dynamic Disorder of Fe<sup>3+</sup> Ions in the Crystal Structure of Natural Barioferrite

Arkadiusz Krz̄at̄ala<sup>1,\*</sup>, Taras L. Panikorovskii<sup>2</sup> , Irina O. Galuskina<sup>1</sup>  
and Evgeny V. Galuskin<sup>1</sup> <sup>1</sup> Faculty of Earth Sciences, University of Silesia, Będzińska 60, 41-200 Sosnowiec, Poland; irina.galuskina@us.edu.pl (I.O.G.); evgeny.galuskin@us.edu.pl (E.V.G.)<sup>2</sup> Kola Science Centre, Russian Academy of Sciences, 14 Fersman street, Apatity 184200, Russia; taras.panikorovsky@spbu.ru

\* Correspondence: akrzatala@us.edu.pl; Tel.: +48-32-368-9689

Received: 13 July 2018; Accepted: 6 August 2018; Published: 8 August 2018



**Abstract:** A natural barioferrite, BaFe<sup>3+</sup><sub>12</sub>O<sub>19</sub>, from a larnite–schorlomite–gehlenite vein of paralava within gehlenite hornfels of the Hatrurim Complex at Har Parsa, Negev Desert, Israel, was investigated by Raman spectroscopy, electron probe microanalysis, and single-crystal X-ray analyses acquired over the temperature range of 100–400 K. The crystals are up to 0.3 mm × 0.1 mm in size and form intergrowths with hematite, magnesioferrite, khesinite, and harmunite. The empirical formula of the barioferrite investigated is as follows: (Ba<sub>0.85</sub>Ca<sub>0.12</sub>Sr<sub>0.03</sub>)<sub>Σ1</sub>(Fe<sup>3+</sup><sub>10.72</sub>Al<sub>0.46</sub>Ti<sup>4+</sup><sub>0.41</sub>Mg<sub>0.15</sub>Cu<sup>2+</sup><sub>0.09</sub>Ca<sub>0.08</sub>Zn<sub>0.04</sub>Mn<sup>2+</sup><sub>0.03</sub>Si<sub>0.01</sub>)<sub>Σ11.99</sub>O<sub>19</sub>. The strongest bands in the Raman spectrum are as follows: 712, 682, 617, 515, 406, and 328 cm<sup>−1</sup>. The structure of natural barioferrite (*P*<sub>63</sub>/*mmc*, *a* = 5.8901(2) Å, *c* = 23.1235(6) Å, *V* = 694.75(4) Å<sup>3</sup>, *Z* = 2) is identical with the structure of synthetic barium ferrite and can be described as an interstratification of two fundamental blocks: spinel-like *S*-modules with a cubic stacking sequence and *R*-modules that have hexagonal stacking. The displacement ellipsoids of the trigonal bipyramidal site show elongation along the [001] direction during heating. As a function of temperature, the mean apical Fe–O bond lengths increase, whereas the equatorial bond lengths decrease, which indicates dynamic disorder at the Fe2 site.

**Keywords:** barioferrite; crystal structure; single-crystal investigation; Raman; Hatrurim Complex

## 1. Introduction

Barioferrite, BaFe<sub>12</sub>O<sub>19</sub>, *P*<sub>63</sub>/*mmc*, *a* = 5.8921(2) Å, *c* = 23.1092(8) Å was described as a new mineral species from a metamorphosed baryte nodule, which was found on the southern slope of Har Ye’elim, a mountain in the Negev Desert, Israel. In this nodule, barioferrite occurs as small platy crystals up to 3 × 15 × 15 μm<sup>3</sup>, as well as their aggregates. Therefore, the unit cell dimensions of the holotype specimen were obtained only from powder X-ray diffraction data [1]. There are several descriptions of synthetic BaFe<sub>12</sub>O<sub>19</sub> [2–5], whereas there are no previous single-crystal structure studies of natural BaFe<sub>12</sub>O<sub>19</sub>.

Barioferrite belongs to the magnetoplumbite group. This group is characterized by the general crystal chemical formula AM<sub>12</sub>O<sub>19</sub>, where *A* = Ba, Pb, K, Ca, Fe<sup>2+</sup>, Mn, Mg, REE and *M* = Fe<sup>2+,3+</sup>, Mg, Al, Ti<sup>4+</sup>, Cr<sup>3+</sup>, Mn<sup>2+,4+</sup>, Zn [6]. Minerals of the magnetoplumbite group are characterized by a modular structure composed of three-layered spinel blocks (*S*) interstratified with *R*-blocks, in which the larger *A*-site cations are located [7].

A natural occurrence of BaFe<sub>12</sub>O<sub>19</sub> was first reported from Si-undersaturated Ca-Fe-rich buchite in porcelanite deposits at Želénky in the North Bohemian Brown Coal Basin, Czech Republic [8].

Our investigations have shown that barioferrite, occurring in small segregations intergrown with other ferrites, is a common accessory mineral of rankinite-bearing paralavas that are hosted by gehlenite hornfelses that belong to the pyrometamorphic Hatrurim Complex [9–11]. Pyrometamorphic rocks of the Hatrurim Complex are distributed in the territory of Israel, the Palestinian Autonomy, and Jordan along the rift of the Dead Sea [12–15].

Synthetic  $\text{BaFe}_{12}\text{O}_{19}$  is well known under such names as barium ferrite, hexaferrite, barium hexaferrite, ferroxdure, M ferrite, and BaM [7]. An X-ray single-crystal study of synthetic  $\text{BaFe}_{12}\text{O}_{19}$  was first undertaken by Townes [16], and the structure was reinvestigated in detail by Obradors [2]. They found that it is isostructural with magnetoplumbite,  $\text{PbFe}^{3+}_{12}\text{O}_{19}$ , which was described by Aminoff (1925) [17] and structurally characterized by Adelsköld in 1938 [7]. Many authors have tried to refine the crystal structure of synthetic  $\text{BaFe}_{12}\text{O}_{19}$  in different space groups (e.g.,  $P-62c$  and  $P6_3mc$ ), and all of them considered space group  $P6_3/mmc$  as the most probable one [2–5]. In space group  $P6_3/mmc$ , the Fe2 site has trigonal bipyramid coordination [18]; this site demonstrates splitting or extreme elongation of the displacement ellipsoid along the [001] direction [2]. The relative displacement of iron from the center of the  $\text{FeO}_5$  bipyramid induces a local electric and dipole moment, which affects the paraelectric/ferroelectric properties of hexaferrites [19].

In this paper, we present the results of the single-crystal structural investigation of natural barioferrite for the first time. Also, powder diffraction data, chemical composition, and single-crystal Raman spectroscopic data are provided for the studied mineral. We pay attention to the structural deformations of the trigonal bipyramidal site at different temperatures and consider mechanisms for the incorporation of Al, Ti, and Mg into the structure of natural barioferrite.

## 2. Methods and Description

### 2.1. Geological Setting and Mineral Description

The barioferrite investigated was found in the outcrops at Har Parsa, which is located in the eastern part of the Hatrurim Basin, about 10 km southeast of Arad, Negev Desert, Israel. The Hatrurim Basin is the one of the largest units in the Hatrurim pyrometamorphic complex. It is a generally recognized fact that the terrigenous-carbonate protolith of the Hatrurim Complex was driven by combustion processes [20–23]. The geology and origin of the Hatrurim Complex have been discussed previously in some detail [21–26]. Many new minerals including aradite, zadovite [9], gurimite, hexacelsian [10], ariegilatite [27], flamite [28], shulamitite [29], barioferrite [1], silicocarnotite [30], and gazeevite [31] have been described from this locality.

Barioferrite forms platy submetallic crystals in a small paralava vein up to 1.5 cm thick in gehlenite hornfels at Har Parsa. Some barioferrite crystals reach  $0.3 \text{ mm} \times 0.1 \text{ mm}$  in size (Figure 1b,c). Minerals of the larnite-flamite and andradite-schorlomite series,  $\text{Fe}^{3+}$ -bearing gehlenite, magnesioferrite, and khesinite, are rock-forming minerals in this paralava (Figure 1a). Barioferrite forms intergrowths with hematite, magnesioferrite  $\text{MgFe}_2\text{O}_4$ , khesinite  $\text{Ca}_4\text{Mg}_2\text{Fe}^{3+}_{10}\text{O}_4(\text{Fe}^{3+}_{10}\text{Si}_2)\text{O}_{36}$  (often with  $\text{Ca} > \text{Mg}$  at the Mg site [11]), and harmunite  $\text{CaFe}_2\text{O}_4$  (Figure 1d) and is also present as small inclusions in gehlenite (Figure 1a). Minor and accessory minerals, in addition to the above-listed ferrites, are represented by vorlanite  $\text{CaUO}_4$ , Si-Fe-bearing perovskite, P-bearing fluorellestadite, and baryte.

### 2.2. Methods of Investigation

The morphology and composition of barioferrite and associated minerals were studied using optical microscopy, scanning electron microscopy (Phenom-World, Eindhoven, The Netherlands) (Phenom XL, Faculty of Earth Sciences, University of Silesia, Sosnowiec, Poland), and an electron probe microanalyzer (Cameca, Gennevilliers, France) (Cameca SX100, Institute of Geochemistry, Mineralogy and Petrology, University of Warsaw, Warsaw, Poland). Elemental analyses were carried out (WDS-mode, 15 kV, 20 nA,  $\sim 1 \mu\text{m}$  beam diameter) using the following X-ray lines (detection limit, wt %) and standards: Si  $K\alpha$  (0.03), Ca  $K\alpha$  (0.04), Mg  $K\alpha$  (0.03)—diopside; Al  $K\alpha$  (0.03)—orthoclase;

Ti  $K\alpha$  (0.05)—TiO<sub>2</sub>; Mn  $K\alpha$  (0.10)—rhodonite; Fe  $K\alpha$  (0.13)—Fe<sub>2</sub>O<sub>3</sub>; Ba  $L\alpha$  (0.11)—baryte; Sr  $L\alpha$  (0.09)—celestine; Cu  $K\alpha$  (0.17)—cuprite; and Zn  $K\alpha$  (0.23)—sphalerite. Corrections were calculated using a PAP procedure provided by CAMECA [32].

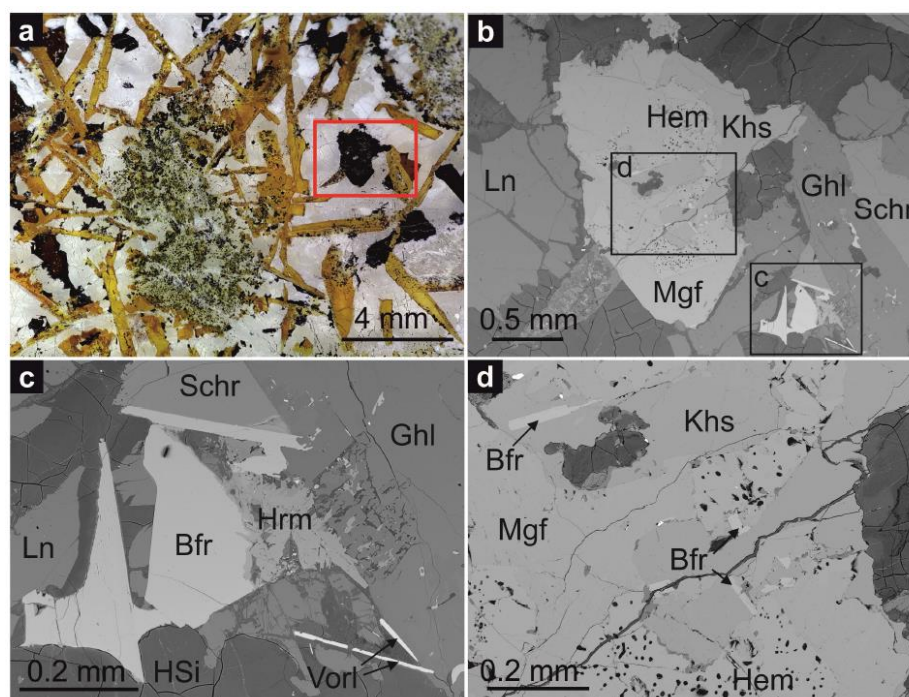


**Figure 1.** (a) Fragments of larnite-gehlenite paralava from Har Parsa with barioferrite aggregates and gehlenite porphyroblasts (megacrysts); fine-grained greenish gehlenite rock occurs in the center. The minerals can be distinguished by color: garnet—dark-brown; gehlenite—orange to yellow-brown; larnite—light-grey to colorless; barioferrite—black; secondary hydrous Ca-silicates—chalk white to light-grey. The area shown in the red frame is magnified in Figure 1b; (b) backscattered-electron (BSE) image of larnite-gehlenite paralava with barioferrite crystals. The framed areas are magnified in Figure 1c,d; (c) subhedral barioferrite crystals with harmunite; (d) aggregate composed of magnesioferrite, hematite, and khesinite with lamellar barioferrite crystals. Labels: Bfr—barioferrite, Ghl—gehlenite, Hem—hematite, Hrm—harmunite, HSi—hydrous silicate, Khs—khesinite, Ln—larnite, Mgf—magnesioferrite, Schr—schorlomite, and Vorl—vorlanite.

The Raman spectra of barioferrite were recorded using a WITec alpha 300R Confocal Raman Microscope (WITec, Ulm, Germany) (Faculty of Earth Sciences, University of Silesia, Sosnowiec, Poland) equipped with an air-cooled solid-state laser (532 nm) and a CCD camera operating at  $-61\text{ }^{\circ}\text{C}$ . The laser radiation was coupled to a microscope through a single-mode optical fiber with a diameter of  $3.5\text{ }\mu\text{m}$ . A Zeiss LD EC Epiplan-Neofluar DIC-100/0.75NA objective was used. Raman scattered light was focused on a broadband single-mode fiber with an effective pinhole size of about  $30\text{ }\mu\text{m}$ , and a monochromator with a  $600\text{ groove/mm}^{-1}$  grating was used. The power of the laser at the sample position was ca.  $25\text{--}30\text{ mW}$ . Integration times of  $10\text{ s}$  with an accumulation of  $20$  scans and a resolution  $3\text{ cm}^{-1}$  were chosen. The monochromator was calibrated using the Raman scattering line of a silicon plate ( $520.7\text{ cm}^{-1}$ ). Spectra processing, such as baseline correction and smoothing, was performed using the SpectraCalc software package GRAMS (Galactic Industries Corporation, Salem, NH, USA). Band-fitting was performed using a Gauss–Lorentz cross-product function, with a minimum number of component bands used for the fitting process.

Powder X-ray diffraction patterns of barioferrite were obtained using a Rigaku R-Axis RAPID II diffractometer (Rigaku Co., Tokyo, Japan) (Saint Petersburg State University, Saint Petersburg, Russia) equipped with a cylindrical image plate detector using the Debye–Scherrer geometry ( $d = 127.4\text{ mm}$ ;

Co  $K\alpha$  radiation) and measured at room temperature. The data were integrated using the software package Osc2Tab/SQRay [33].

The single-crystal X-ray diffraction experiments were carried out at 100, 200, 300, and 400 K using an Agilent Technologies Xcalibur Eos diffractometer (Agilent Technologies, Santa Clara, CA, USA) (Saint Petersburg State University, Saint Petersburg, Russia) operated at 50 kV and 40 mA and equipped with an Oxford Cobra Plus system (Table 1). More than a hemisphere of three-dimensional data was collected using monochromatic Mo  $K\alpha$  X-radiation with frame widths of  $1^\circ$  and 40–80 s count time for each frame. The systematic absences observed are consistent with space group  $P6_3/mmc$ .

**Table 1.** Crystal data and structure refinement for barioferrite at 100, 200, 300, and 400 K.

Identification Code	100 K	200 K	300 K	400 K
Temperature (K)	100(2)	200(2)	300(2)	400(2)
Crystal system, Z	Hexagonal			
Space group	$P6_3/mmc$			
$a$ (Å)	5.8920(2)	5.8901(2)	5.8901(2)	5.8992(2)
$c$ (Å)	23.1092(7)	23.1171(7)	23.1235(6)	23.1891(9)
Volume (Å <sup>3</sup> )	694.78(5)	694.57(4)	694.75(4)	698.87(6)
$\rho_{\text{calc}}$ (g/cm <sup>3</sup> )	5.183	5.184	5.183	5.152
$\mu$ (mm <sup>-1</sup> )	14.131	14.136	14.132	14.049
$F(000)$	1017.0	1017.0	1017.0	1017.0
Crystal size (mm <sup>3</sup> )	0.20 × 0.09 × 0.07			
Radiation	Mo $K\alpha$ ( $\lambda = 0.71073$ )			
2 $\theta$ range (°)	7.054–64.038	7.05–63.804	7.048–61.54	7.028–64.436
$hkl$ range	$-8 \leq h \leq 8, -6 \leq k \leq 6, -33 \leq l \leq 33$	$-8 \leq h \leq 8, -8 \leq k \leq 8, -32 \leq l \leq 32$	$-7 \leq h \leq 7, -8 \leq k \leq 8, -32 \leq l \leq 28$	$-8 \leq h \leq 8, -7 \leq k \leq 8, -32 \leq l \leq 32$
Reflections collected	3907	6363	6065	6804
Independent reflections	501 [ $R_{\text{int}} = 0.0176$ , $R_{\text{sigma}} = 0.0106$ ]	505 [ $R_{\text{int}} = 0.0300$ , $R_{\text{sigma}} = 0.0148$ ]	461 [ $R_{\text{int}} = 0.0281$ , $R_{\text{sigma}} = 0.0121$ ]	519 [ $R_{\text{int}} = 0.0279$ , $R_{\text{sigma}} = 0.0118$ ]
Data/restraints/parameters	501/0/42	508/0/42	461/0/42	519/0/42
Goof	1.229	1.270	1.288	1.268
Final $R$ indexes [ $I \geq 2\sigma(I)$ ]	$R_1 = 0.0142$ , $wR_2 = 0.0364$	$R_1 = 0.0207$ , $wR_2 = 0.0493$	$R_1 = 0.0161$ , $wR_2 = 0.0425$	$R_1 = 0.0173$ , $wR_2 = 0.0433$
Final $R$ indexes [all data]	$R_1 = 0.0164$ , $wR_2 = 0.0372$	$R_1 = 0.0234$ , $wR_2 = 0.0506$	$R_1 = 0.0179$ , $wR_2 = 0.0431$	$R_1 = 0.0193$ , $wR_2 = 0.0440$
Largest difference peak/hole (e Å <sup>-3</sup> )	0/53/−0.56	1.13/−0.99	0.43/−0.89	0.79/−1.16

### 2.3. Chemical Composition and Raman Spectroscopy

To identify barioferrite, we performed electron probe microanalysis and Raman spectroscopy. Barioferrite from the paralava of Har Parsa has a relatively constant composition and contains substantial substitutional elements, including Ti<sup>4+</sup>, Al, and Ca (Table 2). The presence of Cu and Zn and also the interpreted incorporation of small amounts of Ca in the spinel module is a specific feature not only of barioferrite from Har Parsa paralava, but also barioferrite and magnesioferrite from other localities of pyrometamorphic rocks of the Hatrurim Complex [11,29,34]. The positive charge caused by substituted trivalent iron by tetravalent titanium is compensated by the presence of divalent elements. The empirical crystal chemical formula of barioferrite is as

follows:  $(\text{Ba}_{0.85}\text{Ca}_{0.12}\text{Sr}_{0.03})_{\Sigma 1}(\text{Fe}^{3+}_{10.72}\text{Al}_{0.46}\text{Ti}^{4+}_{0.41}\text{Mg}_{0.15}\text{Cu}^{2+}_{0.09}\text{Ca}_{0.08}\text{Zn}_{0.04}\text{Mn}^{2+}_{0.03}\text{Si}_{0.01})_{\Sigma 11.99}\text{O}_{19}$ . This composition of barioferrite is close to the end-member  $\text{BaFe}_{12}\text{O}_{19}$ .

In the barioferrite structure, the spinel blocks are composed of  $\text{Fe}^{(3)}\text{O}_4$  tetrahedra and  $\text{Fe}^{(1,4)}\text{O}_6$  octahedra, whereas *R*-blocks are formed by  $\text{Fe}^{(2)}\text{O}_5$  trigonal bipyramids and  $\text{Fe}^{(5)}\text{O}_6$  octahedra with dodecaordinated Ba in structural cages. The main bands observed in the Raman spectra of the studied barioferrite are associated with  $\text{Fe}^{3+}\text{O}$  vibrations and shifted towards the higher Raman shift frequency in comparison with analogous bands of synthetic barioferrite (our data, Figure 2/synthetic barioferrite [35],  $\text{cm}^{-1}$ ): 714/713 [ $A_{1g}$ , tetrahedron  $\text{Fe}^{(3)}\text{O}_4$ ]; 689/684 [ $A_{1g}$ , bipyramid  $\text{Fe}^{(2)}\text{O}_5$ ]; 624/614 [ $A_{1g}$ , octahedron  $\text{Fe}^{(5)}\text{O}_6$ ]; 532/527, 520/512 [ $A_{1g}$ , octahedron  $\text{Fe}^{(1)}\text{O}_6$  and  $\text{Fe}^{(4)}\text{O}_6$ ]; 412/409 [ $A_{1g}$ ,  $\text{Fe}^{(4)}\text{O}_6$  octahedron dominated]; 335/335 + 317 [ $E_{1g}$  +  $E_{2g}$ ]. Similar band shifts were observed in Raman spectrum of synthetic barioferrite  $\text{Ba}_{1-x}\text{Ca}_x\text{Fe}_{12}\text{O}_{19}$ , with  $x = 0.1$  [36]. In the studied barioferrite, 0.12 Ca pfu is present at the Ba site (Table 2), which most probably determines the band shifts. Also, we cannot exclude an influence of Al and  $\text{Ti}^{4+}$  impurities substituting for  $\text{Fe}^{3+}$  (Table 2) on bands position in the Raman spectrum. A similar effect was described before for Ti-bearing synthetic barioferrite [37]. Moreover, wide band centered about  $1359 \text{ cm}^{-1}$  is overtone (Figure 2). The bands at 164 and  $178 \text{ cm}^{-1}$  are assigned to the motion of the spinel block as a whole [35]. The band near  $673 \text{ cm}^{-1}$  is not usually noted in barioferrite spectra [35,37]; it was observed once in the spectrum of pure barioferrite [38], and it is possible, that this band is related to  $\text{Fe}^{3+}$  in the bipyramid.

**Table 2.** Chemical composition of barioferrite from Har Parsa.

Component (wt %)	Mean ( $n = 17$ )	Range	Standard Deviation.	Calculated on 19 O	
TiO <sub>2</sub>	3.05	2.90–3.27	0.09	Ba	0.85
SiO <sub>2</sub>	0.05	0.00–0.10	0.02	Ca	0.12
Fe <sub>2</sub> O <sub>3</sub>	80.47	78.89–81.53	0.72	Sr	0.03
Al <sub>2</sub> O <sub>3</sub>	2.22	2.11–2.38	0.06	<b>A site</b>	<b>1</b>
BaO	12.32	11.56–13.41	0.46	Fe <sup>3+</sup>	10.72
MgO	0.58	0.51–0.68	0.05	Al	0.46
CaO	1.03	0.83–1.32	0.17	Ti	0.41
MnO	0.18	0.11–0.23	0.04	Mg	0.15
SrO	0.32	0.14–0.43	0.07	Cu <sup>2+</sup>	0.09
CuO	0.65	0.48–0.84	0.11	Ca	0.08
ZnO	0.33	0.19–0.47	0.08	Zn	0.04
	101.2	100.09–101.69		Mn <sup>2+</sup>	0.03
				Si	0.01
				<b>M sites</b>	<b>11.99</b>

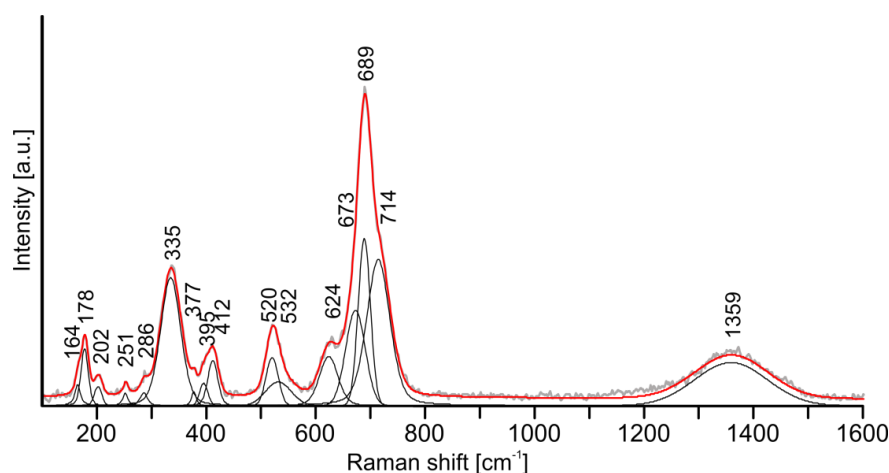


**Figure 2.** Raman spectrum of barioferrite from Har Parsa; grain is shown in Figure 1c.

### 3. X-ray Diffraction Studies

#### 3.1. Powder Diffraction Data

All peaks in the powder spectra (Figure 3) of barioferrite correspond to the synthetic  $\text{BaFe}_{12}\text{O}_{0.19}$  (PDF-2, card number 01-084-0757). The unit-cell parameters refined from these data are as follows:  $P6_3/mmc$ ,  $a = 5.8908(1) \text{ \AA}$ ,  $c = 23.1334(6) \text{ \AA}$ ,  $V = 694.91(3) \text{ \AA}^3$ , and  $Z = 2$ , which are in good agreement with the single-crystal data  $a = 5.8901(6) \text{ \AA}$ ,  $c = 23.1235(6) \text{ \AA}$ , and  $V = 694.75(4) \text{ \AA}^3$  obtained at 300 K. There are no additional superstructure reflections, as observed in [39].

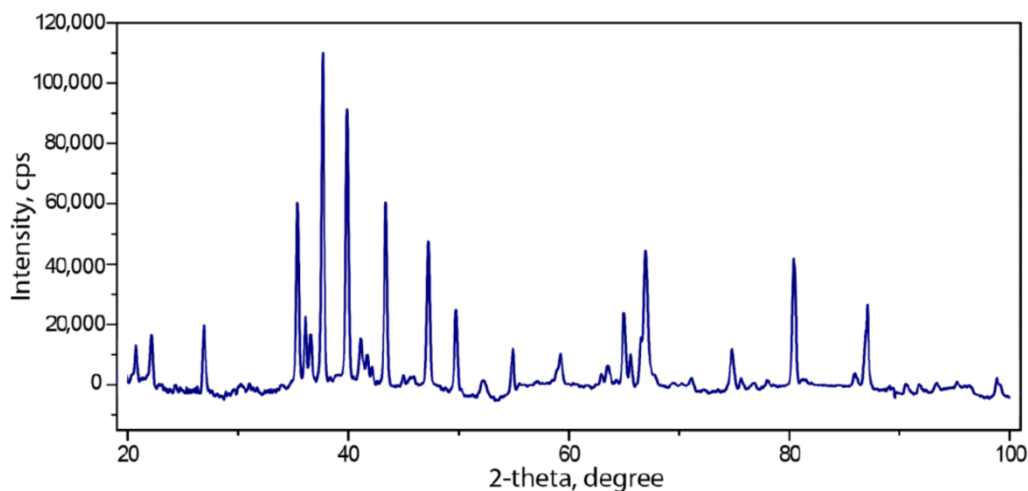


Figure 3. Powder diffraction spectra of barioferrite.

#### 3.2. Single-Crystal X-ray Diffraction Data

A fragment of the barioferrite crystal shown in Figure 1c was used for the single-crystal structural investigations. The experimental details and crystallographic parameters are given in Table 1. The crystal structure of barioferrite was refined with the use of the *SHELX* program [40]. Empirical absorption corrections were applied in the *CrysAlisPro* [41] suite of programs using spherical harmonics, implemented in the *SCALE3 ABSPACK* scaling algorithm. The volumes of coordination polyhedra were calculated using the *VESTA 3* program [42]. Atomic labels were assigned following the first crystal structure description [3]. The final atomic coordinates and isotropic displacement parameters are reported in Table 3, selected interatomic distances are in Table 4, and anisotropic displacement parameters are given in the Table 5. Table 6 provides information on the polyhedral volumes of cations.

**Table 3.** Atomic coordinates, displacement parameters ( $\text{\AA}^2$ ), and site occupancies for barioferrite at 100, 200, 300, and 400 K.

Temperature:		100 K					200 K				
Site	population	$x/a$	$y/b$	$z/c$	$U_{\text{eq}}$	Population	$x/a$	$y/b$	$z/c$	$U_{\text{eq}}$	
Ba1	Ba <sub>0.89</sub> Ca <sub>0.011</sub>	2/3	1/3	1/4	0.0038(1)	Ba <sub>0.89</sub> Ca <sub>0.011</sub>	2/3	1/3	1/4	0.0063(1)	
Fe1	Fe <sub>0.69</sub> Al <sub>0.31</sub>	0	0	0	0.0020(3)	Fe <sub>0.69</sub> Al <sub>0.31</sub>	0	0	0	0.0038(2)	
Fe2	Fe <sub>0.96</sub> Ti <sub>0.04</sub>	0	0	1/4	0.0116(2)	Fe <sub>0.96</sub> Ti <sub>0.04</sub>	0	0	1/4	0.0154(2)	
Fe3	Fe <sub>0.94</sub> Mg <sub>0.06</sub>	1/3	2/3	0.02730(3)	0.0025(1)	Fe <sub>0.94</sub> Mg <sub>0.06</sub>	1/3	2/3	0.02729(3)	0.0043(2)	
Fe4	Fe <sub>0.94</sub> Ti <sub>0.06</sub>	0.33617(8)	0.16809(4)	0.10792(2)	0.0026(1)	Fe <sub>0.94</sub> Ti <sub>0.06</sub>	0.33622(7)	0.16811(4)	0.10789(2)	0.0044(1)	
Fe5	Fe	1/3	2/3	0.18977(3)	0.0031(1)	Fe	1/3	2/3	0.18974(3)	0.0047(2)	
O1	O	0	0	0.1514(1)	0.0043(5)	O	0	0	0.15126(14)	0.0057(6)	
O2	O	2/3	1/3	0.0555(1)	0.0037(5)	O	2/3	1/3	0.05564(15)	0.0054(6)	
O3	O	0.5022(2)	0.0043(3)	0.1496(1)	0.0035(3)	O	0.5022(2)	0.0044(4)	0.14967(8)	0.0056(4)	
O4	O	0.1543(2)	0.3086(3)	0.05198(5)	0.0050(3)	O	0.15399(19)	0.3080(4)	0.05197(9)	0.0062(4)	
O5	O	0.1825(2)	0.3651(5)	1/4	0.0051(4)	O	0.1825(3)	0.3649(5)	1/4	0.0066(5)	
Temperature:		300 K					400 K				
Site	population	$x/a$	$y/b$	$z/c$	$U_{\text{eq}}$	population	$x/a$	$y/b$	$z/c$	$U_{\text{eq}}$	
Ba1	Ba <sub>0.89</sub> Ca <sub>0.011</sub>	2/3	1/3	1/4	0.0082(1)	Ba <sub>0.89</sub> Ca <sub>0.011</sub>	2/3	1/3	1/4	0.0104(1)	
Fe1	Fe <sub>0.69</sub> Al <sub>0.31</sub>	0	0	0	0.0049(2)	Fe <sub>0.69</sub> Al <sub>0.31</sub>	0	0	0	0.0063(2)	
Fe2	Fe <sub>0.96</sub> Ti <sub>0.04</sub>	0	0	1/4	0.0184(3)	Fe <sub>0.96</sub> Ti <sub>0.04</sub>	0	0	1/4	0.0222(3)	
Fe3	Fe <sub>0.94</sub> Mg <sub>0.06</sub>	1/3	2/3	0.0272(3)	0.0052(2)	Fe <sub>0.94</sub> Mg <sub>0.06</sub>	1/3	2/3	0.02729(3)	0.0066(1)	
Fe4	Fe <sub>0.94</sub> Ti <sub>0.06</sub>	0.33623(7)	0.16811(4)	0.10789(2)	0.00563(14)	Fe <sub>0.94</sub> Ti <sub>0.06</sub>	0.33624(7)	0.16812(4)	0.10789(2)	0.00720(11)	
Fe5	Fe	1/3	2/3	0.18975(3)	0.0055(1)	Fe	1/3	2/3	0.18972(3)	0.00744(14)	
O1	O	0	0	0.15107(13)	0.0063(6)	O	0	0	0.1509(1)	0.0079(6)	
O2	O	2/3	1/3	0.0557(1)	0.0063(6)	O	2/3	1/3	0.0557(1)	0.0076(6)	
O3	O	0.5022(2)	0.0044(3)	0.14958(7)	0.0064(4)	O	0.5024(2)	0.0048(4)	0.14951(8)	0.0083(3)	
O4	O	0.1541(2)	0.3082(4)	0.05206(8)	0.0073(4)	O	0.1542(2)	0.3084(4)	0.05187(8)	0.0088(3)	
O5	O	0.1821(3)	0.3643(5)	1/4	0.0080(5)	O	0.1820(3)	0.3639(5)	1/4	0.0098(5)	

The refined formula is: (Ba<sub>0.89</sub>Ca<sub>0.11</sub>)<sub>1.00</sub>(Fe<sub>11.17</sub>Ti<sub>0.40</sub>Al<sub>0.31</sub>Mg<sub>0.12</sub>)<sub>12.00</sub>O<sub>19</sub>.

**Table 4.** Selected bond distances (Å) for the crystal structures of barioferrite at 100, 200, 300, and 400 K.

Temperature Bond		100 K Mean	Temperature Bond		200 K Mean	Temperature Bond		300 K Mean	Temperature Bond		400 K Mean
Ba1-O3	x6	2.8624(16)	Ba1-O3	x6	2.8624(19)	Ba1-O3	x6	2.8646(18)	Ba1-O3	x6	2.8711(18)
Ba1-O5	x6	2.9505(2)	Ba1-O5	x6	2.9495(2)	Ba1-O5	x6	2.9493(16)	Ba1-O5	x6	2.9537(2)
<Ba1-O>		2.9061	<Ba1-O>		2.906	<Ba1-O>		2.907	<Ba1-O>		2.913
Fe1-O4	x6	1.980(2)	Fe1-O4	x6	1.9782(19)	Fe1-O4	x6	1.9796(19)	Fe1-O4	x6	1.9822(18)
Fe2-O1	x2	2.278(3)	Fe2-O1	x2	2.283(3)	Fe2-O1	x2	2.288(3)	Fe2-O1	x2	2.298(3)
Fe2-O5	x3	1.863(2)	Fe2-O5	x3	1.862(3)	Fe2-O5	x3	1.858(3)	Fe2-O5	x3	1.859(3)
<Fe2-O>		2.028	<Fe2-O>		2.030	<Fe2-O>		2.041	<Fe2-O>		2.034
Fe3-O2		1.914(3)	Fe3-O2		1.917(4)	Fe3-O2		1.916(2)	Fe3-O2		1.922(3)
Fe3-O4	x3	1.914(2)	Fe3-O4	x3	1.917(2)	Fe3-O4	x3	1.915(4)	Fe3-O4	x3	1.9167(19)
<Fe3-O>		1.914	<Fe3-O>		1.917	<Fe3-O>		1.917	<Fe3-O>		1.919
Fe4-O1		1.9886(5)	Fe4-O1		1.9867(17)	Fe4-O1		1.9847(16)	Fe4-O1		1.9866(17)
Fe4-O2		2.0757(17)	Fe4-O2		2.074(2)	Fe4-O2		2.0750(19)	Fe4-O2		2.0783(19)
Fe4-O3	x2	1.9399(10)	Fe4-O3	x2	1.9394(12)	Fe4-O3	x2	1.9385(12)	Fe4-O3	x2	1.9406(12)
Fe4-O4	x2	2.0956(12)	Fe4-O4	x2	2.0943(15)	Fe4-O4	x2	2.0949(13)	Fe4-O4	x2	2.1013(14)
<Fe4-O>		2.022	<Fe4-O>		2.021	<Fe4-O>		2.020	<Fe4-O>		2.025
Fe5-O3	x3	1.9562(16)	Fe5-O3	x3	1.9560(19)	Fe5-O3	x3	1.9574(19)	Fe5-O3	x3	1.9629(18)
Fe5-O5	x3	2.0749(18)	Fe5-O5	x3	2.076(2)	Fe5-O5	x3	2.078(12)	Fe5-O5	x3	2.0847(19)
<Fe5-O>		2.016	<Fe5-O>		2.016	<Fe5-O>		2.018	<Fe5-O>		2.024

**Table 5.** Anisotropic displacement parameters ( $\text{\AA}^2$ ) for the structure of barioferrite.

100 K												
Atom	$U^{11}$	$U^{22}$	$U^{33}$	$U^{23}$	$U^{13}$	$U^{12}$	$U^{11}$	$U^{22}$	$U^{33}$	$U^{23}$	$U^{13}$	$U^{12}$
Ba1	0.00371(12)	0.00371(12)	0.00389(17)	0.000	0.000	0.00186(6)	0.00695(15)	0.00695(15)	0.0050(2)	0.000	0.000	0.00348(8)
Fe1	0.0024(2)	0.0024(2)	0.0010(4)	0.000	0.000	0.00121(12)	0.0051(3)	0.0051(3)	0.0014(4)	0.000	0.000	0.00253(15)
Fe2	0.0012(2)	0.0012(2)	0.0323(6)	0.000	0.000	0.00062(11)	0.0032(3)	0.0032(3)	0.0400(7)	0.000	0.000	0.00159(14)
Fe3	0.00195(17)	0.00195(17)	0.0037(3)	0.000	0.000	0.00097(8)	0.0042(2)	0.0042(2)	0.0043(3)	0.000	0.000	0.00212(11)
Fe4	0.00195(16)	0.00214(13)	0.00356(16)	−0.00001(6)	−0.00003(11)	0.00098(8)	0.0042(2)	0.00473(17)	0.0041(2)	−0.00010(6)	−0.00021(12)	0.00211(10)
Fe5	0.00272(17)	0.00272(17)	0.0038(3)	0.000	0.000	0.00136(8)	0.0052(2)	0.0052(2)	0.0039(3)	0.000	0.000	0.00258(10)
O1	0.0032(7)	0.0032(7)	0.0064(12)	0.000	0.000	0.0016(4)	0.0054(9)	0.0054(9)	0.0064(14)	0.000	0.000	0.0027(4)
O2	0.0030(7)	0.0030(7)	0.0051(12)	0.000	0.000	0.0015(4)	0.0061(9)	0.0061(9)	0.0042(14)	0.000	0.000	0.0030(5)
O3	0.0022(5)	0.0034(7)	0.0054(7)	0.0009(6)	0.0004(3)	0.0017(3)	0.0051(6)	0.0059(8)	0.0059(9)	0.0011(6)	0.0005(3)	0.0030(4)
O4	0.0049(5)	0.0053(7)	0.0050(7)	0.0010(6)	0.0005(3)	0.0026(4)	0.0068(6)	0.0073(9)	0.0047(9)	0.0008(7)	0.0004(3)	0.0036(5)
O5	0.0052(8)	0.0033(10)	0.0062(10)	0.000	0.000	0.0016(5)	0.0092(10)	0.0055(13)	0.0039(12)	0.000	0.000	0.0028(6)
300 K												
Atom	$U^{11}$	$U^{22}$	$U^{33}$	$U^{23}$	$U^{13}$	$U^{12}$	$U^{11}$	$U^{22}$	$U^{33}$	$U^{23}$	$U^{13}$	$U^{12}$
Ba1	0.00855(16)	0.00855(16)	0.0075(2)	0.000	0.000	0.00428(8)	0.01059(14)	0.01059(14)	0.01000(19)	0.000	0.000	0.00529(7)
Fe1	0.0060(3)	0.0060(3)	0.0026(4)	0.000	0.000	0.00300(15)	0.0074(3)	0.0074(3)	0.0041(4)	0.000	0.000	0.00371(14)
Fe2	0.0036(3)	0.0036(3)	0.0480(8)	0.000	0.000	0.00179(14)	0.0044(3)	0.0044(3)	0.0579(8)	0.000	0.000	0.00219(13)
Fe3	0.0050(2)	0.0050(2)	0.0056(3)	0.000	0.000	0.00251(11)	0.00611(19)	0.00611(19)	0.0076(3)	0.000	0.000	0.00305(9)
Fe4	0.0048(2)	0.00538(17)	0.00608(19)	−0.00019(7)	−0.00037(13)	0.00239(10)	0.00589(18)	0.00685(14)	0.00853(18)	−0.00031(6)	−0.00062(12)	0.00295(9)
Fe5	0.0062(2)	0.0062(2)	0.0056(3)	0.000	0.000	0.00312(11)	0.00755(18)	0.00755(18)	0.0072(3)	0.000	0.000	0.00377(9)
O1	0.0054(9)	0.0054(9)	0.0083(13)	0.000	0.000	0.0027(5)	0.0068(8)	0.0068(8)	0.0100(13)	0.000	0.000	0.0034(4)
O2	0.0066(9)	0.0066(9)	0.0057(14)	0.000	0.000	0.0033(5)	0.0075(8)	0.0075(8)	0.0079(13)	0.000	0.000	0.0038(4)
O3	0.0060(6)	0.0060(9)	0.0074(8)	0.0020(7)	0.0010(3)	0.0030(4)	0.0068(5)	0.0078(8)	0.0107(8)	0.0025(6)	0.0012(3)	0.0039(4)
O4	0.0077(6)	0.0078(9)	0.0065(8)	0.0005(7)	0.0003(3)	0.0039(5)	0.0091(6)	0.0093(8)	0.0081(8)	0.0006(6)	0.0003(3)	0.0047(4)
O5	0.0104(10)	0.0054(13)	0.0066(11)	0.000	0.000	0.0027(6)	0.0125(9)	0.0062(12)	0.0085(11)	0.000	0.000	0.0031(6)
400 K												

**Table 6.** Data of polyhedral volumes in the crystal structure of barioferrite at 100, 200, 300, and 400 K.

Polyhedron	Vol. (Å <sup>3</sup> ) 100 K	Vol. (Å <sup>3</sup> ) 200 K	Vol. (Å <sup>3</sup> ) 300 K	Vol. (Å <sup>3</sup> ) 400 K
Ba1	57.060	57.045	57.124	57.463
Fe1	10.318	10.273	10.304	10.340
Fe2	6.847	6.849	6.841	6.877
Fe3	3.591	3.606	3.596	3.615
Fe4	10.908	10.886	10.882	10.941
Fe5	10.680	10.687	10.720	10.815

The site labels and atomic positions were taken from [3], and the crystal structure was refined anisotropically to  $R_1 = 0.014, 0.021, 0.016,$  and  $0.017$  for 501, 508, 461, and 519 unique observed reflections with  $|F_o| \geq 4\sigma_F$  at 100, 200, 300, and 400 K, respectively (Supplementary materials). The thermal ellipsoid of the Fe2 site shows elongation along the [001] direction (Table 5) at 100 K, and additional experiments at 200, 300, and 400 K were performed in order to check the thermal behavior of this site. In contrast to hibonite [43], the model where Fe2 split into two  $4e$  sites does not improve  $R_1$  values. In the split model, during refinement, both  $4e$  sites shift into the central  $2b$  position. In this model, the anisotropic displacement parameters will be more reasonable in character, but due to the short Fe2–Fe2 distance of  $0.277(2)$  Å, their thermal ellipsoids overlapped. Because modern refinements of magnetoplumbite-type structures use a split model, we choose the model with the one central Fe2 atom for convenience of calculation of the polyhedral volumes.

The crystal structure of barioferrite belongs to the magnetoplumbite-type structure (Figure 4). In the terms of close packing, it can be described as the stacking of cubic and hexagonal pack layers in the sequence ... **BAB'ABCAC'AC** ... along the [001] direction [5]. The layers **A**, **B**, and **C** consist exclusively of oxide ions, while the layers **B'** and **C'** are represented by the  $(\text{BaO}_3)^4$  layers [5,44]. In the view of modular crystallography, the crystal structure of barioferrite consist of two fundamental blocks (Figure 4): spinel-like *S*-modules with a cubic stacking sequence of close packed layers and *R*-modules with a hexagonal stacking sequence [2]. *S*-modules consist of a spinel structure fragment, which is based on the two identical sheets of edge-shared Fe4 octahedra and one octahedral (Fe1)/tetrahedral (Fe3) layer embedded between two octahedral layers. The *S*-module contains three independent iron Fe1 ( $2a$ ), Fe3 ( $4f$ ), and Fe4 ( $12k$ ) sites. The Al atoms are incorporated onto the Fe1 site, for which the refined occupancy at 100 K is  $\text{Fe}_{0.69}\text{Al}_{0.31}$ . The polyhedral volume of the Fe1 octahedron is significantly smaller than the other octahedral sites (Figure 5), and the Fe1–O bond length is  $1.980$  Å (100 K), also consistent with the admixture of aluminum. The tetrahedral Fe3 and octahedral Fe4 sites have admixtures of Mg and Ti, respectively. Their mean Fe–O bond lengths are  $1.915$  and  $2.022$  Å (at 100 K) and are consistent with the refined occupancies of  $\text{Fe}_{0.94}\text{Mg}_{0.06}$  and  $\text{Fe}_{0.94}\text{Ti}_{0.06}$ . These bond lengths are close to those theoretically expected,  $1.87$  and  $2.05$  Å [45], respectively, and close to those observed in synthetic barioferrite:  $1.888$  and  $2.007$  Å, respectively [2].

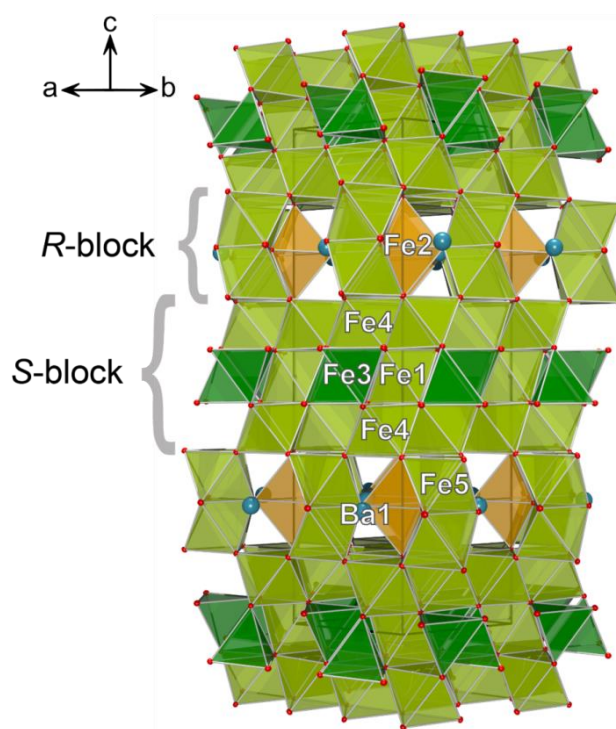


**Figure 4.** Crystal structure of barioferrite at 100 K. The arrangement of iron-centered polyhedra: octahedral—light green, tetrahedra—dark green, and trigonal bipyramid—orange, and the blue spheres represent Ba.

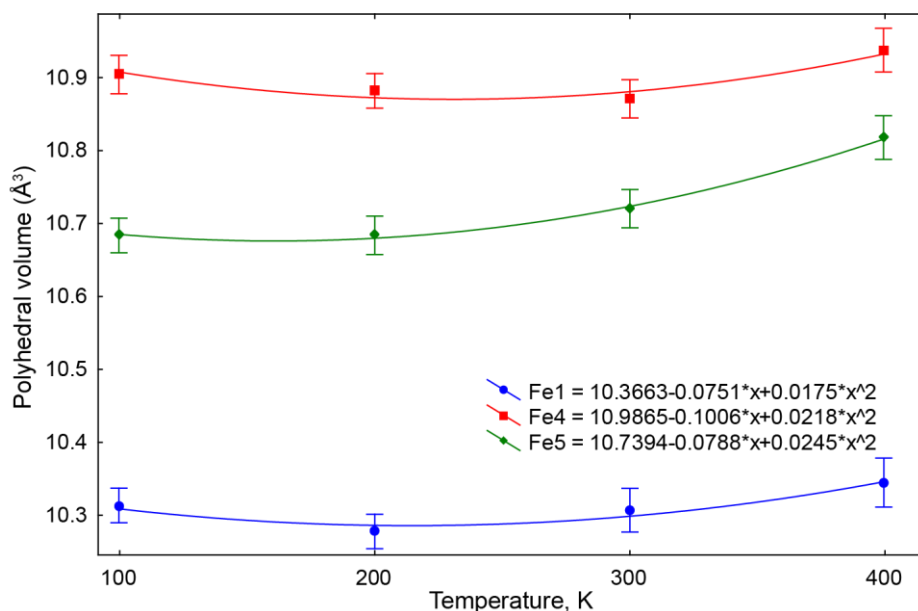


**Figure 5.** Polyhedral volumes of Fe1, Fe4, and Fe5 octahedra in the crystal structure of barioferrite at 100, 200, 300, and 400 K, respectively.

Each *R*-module contains layers formed by face-shared ( $\text{Fe}_2\text{O}_9$ ) octahedra (Fe5 site) that are connected by their apical vertexes with ( $\text{FeO}_5$ ) trigonal bipyramids (Fe2 site). These layers include cavities  $5.89 \times 5.89 \text{ \AA}$  filled by Ba (Ba1) cations. The twelve-coordinated Ba1 site (*2d*) has an admixture of Ca, its refined occupancy is  $\text{Ba}_{0.904}\text{Ca}_{0.096}$  at 100 K. The refined occupancy of the Fe2 site is  $\text{Fe}_{0.96}\text{Ti}_{0.04}$ . The Fe5 (*4f*) and Fe2 (*2b*) sites have mean Fe–O bond lengths of 2.016 and 2.028  $\text{\AA}$ , which are consistent

with magnetoplumbite-type compounds [5,18,46]. The admixtures of Sr, Cu, Ca, Zn, Mn, and Si with an amount lower than 0.1 *apfu* were not determined during refinement; their incorporation is discussed below.

The refined formula of barioferrite can be written as  $\text{Ba}^1(\text{Ba}_{0.89}\text{Ca}_{0.11})^{\text{Fe}1}(\text{Fe}_{0.69}\text{Al}_{0.31})^{\text{Fe}2}(\text{Fe}_{0.96}\text{Ti}_{0.04})^{\text{Fe}3}(\text{Fe}_{1.88}\text{Mg}_{0.12})^{\text{Fe}4}(\text{Fe}_{5.64}\text{Ti}_{0.36})^{\text{Fe}5}(\text{Fe}_{2.00})\text{O}_{19}$  or simplified as  $(\text{Ba}_{0.89}\text{Ca}_{0.11})_{1.00}(\text{Fe}_{11.17}\text{Ti}_{0.40}\text{Al}_{0.31}\text{Mg}_{0.12})_{12.00}\text{O}_{19}$ .

#### 4. Discussion

The natural samples of hexaferrites are of interest to chemists and mineralogists due to the wide range of substitutions, which affect the physical-chemical properties of the titled compounds [43,47]. The present study confirms the incorporation of Mg into the tetrahedral Fe3 site as suggested in [43,48]. The mean Fe–O bond length of 1.914 Å was slightly higher than that in the synthetic barioferrite of 1.888 Å [2]. The incorporation of Ti into magnetoplumbite-like compounds are widely discussed in the literature; according to this data Ti orders into M2 and M4 [49,50] or  $\text{Fe}_4 > \text{Fe}_3 > \text{Fe}_2$  [5]. In our case, Ti is allocated in the Fe2 and Fe4 sites. The polyhedral volume of Fe4 octahedra is significantly larger than other octahedral sites (Figure 5) because of the presence of admixtures of divalent cations, such as Cu, Ca, Zn, and Mn.

With the increase of temperature over the range of 100–300 K, most polyhedra in the structure of natural barioferrite do not significantly change in volume (Tables 5 and 6). That is in agreement with the observations of the magnetoelectric effect in some magnetoplumbite-like compounds at temperatures up to ambient [51]. However, the local negative thermal expansion (NTE) of Fe1 and Fe4 octahedra in the S-block of the structure at the temperatures 100–200 and 100–300 K, respectively—probably, due to local structure deformations—requires further investigation.

The most difficult question is the character of the disorder in the Fe2 site (Figure 6). According to [2,5,52], there are three different models, which can be considered for the structural and dynamic characteristics of the bipyramidal  $\text{Fe}^{3+}$  ions: (1) a non-disordered configuration, (2) a static disorder between two adjacent pseudotetrahedral sites, and (3) a dynamical disorder between these sites (Figure 7).

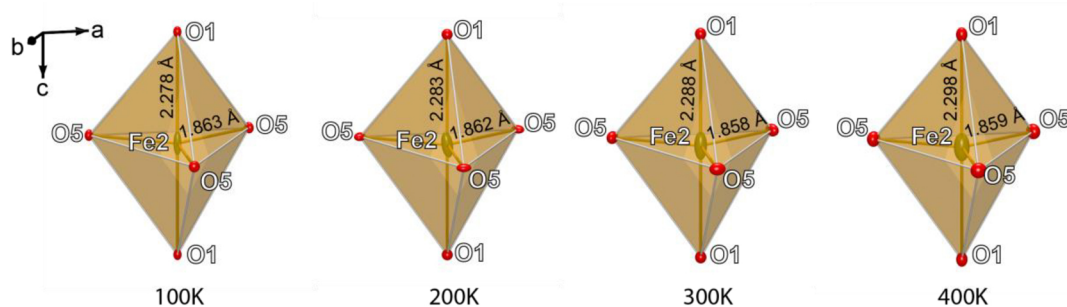


**Figure 6.** Fe2 trigonal bipyramid and Fe–O bond lengths at 100, 200, 300, and 400 K, respectively. Displacement ellipsoids are drawn at the 50% probability level.

It seems that both refinement models support a dynamic disorder character (Figure 8). In the single-atom model, the elongation of the displacement ellipsoid of the iron atom in the trigonal bipyramid along the [001] direction increased with temperature (Table 5). The decrease of the Fe2–O5 distances from 1.862(3) at 100 K to 1.857(3) Å at 400 K was correlated to the increase of the Fe2–O1 distances from 2.279(3) at 100 K to 2.300(3) Å at 400 K. According to our data, the iron atoms were randomly displaced from the center of the trigonal bipyramid. In this case, both structural models were appropriate (Figure 7). In the split-atom model, the Fe2–Fe2 distance increased from 0.277(2) at 100K to 0.358(7) Å at 400 K. In the static model of disorder, the site on the one side of the triangle (O5–O5–O5) plane is occupied by tetrahedrally coordinated Fe, whereas the site on the other side of

the plane is vacant. In our case, the changes of the bond lengths of the FeO<sub>5</sub> polyhedra are significantly smaller for the static model of splitting the Fe2 site, and all attempts to refine the model with a split Fe2 site (situated on the center of the tetrahedra) leads to a significant increase of the R-values. We consider that the disorder at the trigonal bipyramid in the barioferrite crystal structure has an exclusively dynamic disorder character.

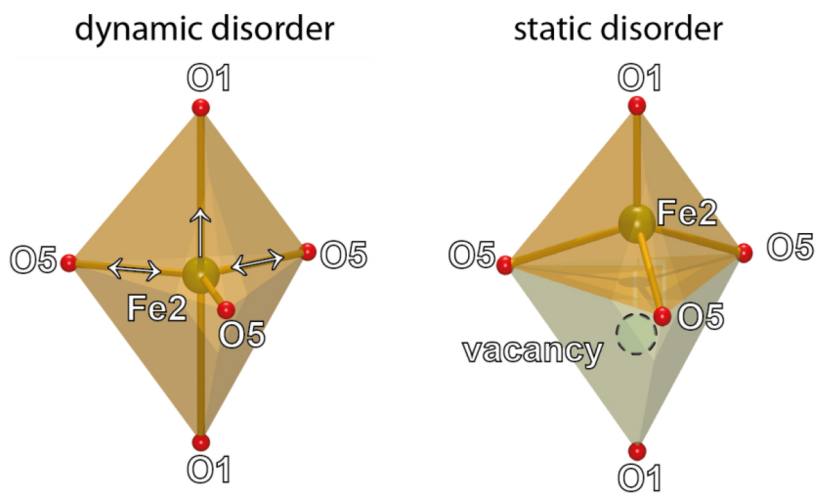


**Figure 7.** Theoretical models of arrangement of the Fe2 site in the barioferrite crystal structure. Arrows shows direction of the bond elongation.

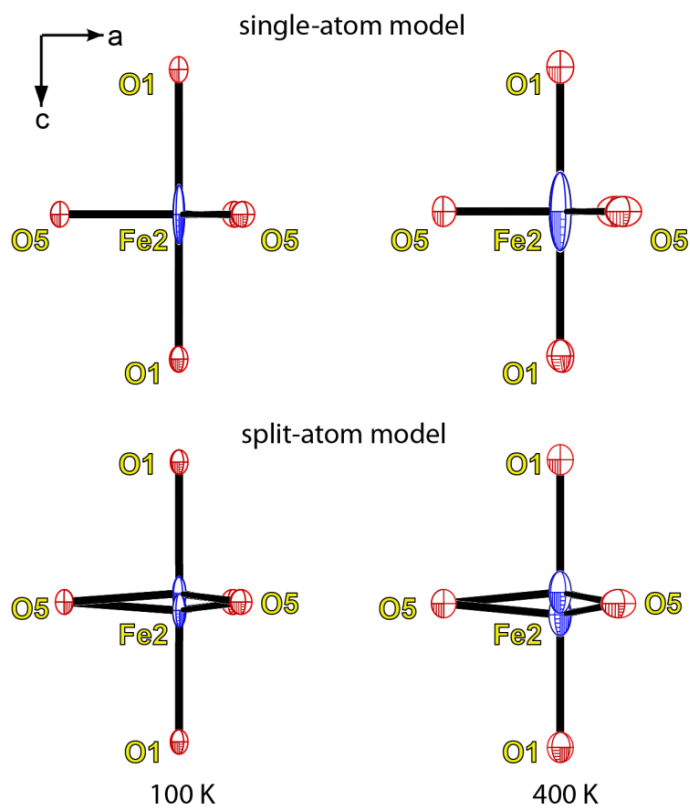


**Figure 8.** Thermal ellipsoids of Fe2, O1, and O5 atoms at 100 and 400 K. Thermal ellipsoids are drawn at the 90% probability level.

In conclusion, it should be noted that although barioferrite was first discovered in an altered baryte nodule and considered to be a very rare mineral [1], it turned out to be a common accessory mineral of high-calcium paralavas and gehlenite hornfelses [9,11]. The natural occurrence of the Ca-analogue of barioferrite (or Fe-analogue of hibonite)  $\text{CaFe}_{12}\text{O}_{19}$  has been recently reported [11], and in addition to barioferrite with a S/R = 3:1 module ratio, a barium ferrite with the S/R = 5:1 ratio  $\text{Ba}(\text{Fe}^{2+}, \text{Mg})_2\text{Fe}_{16}\text{O}_{27}$  also exists [53].

**Supplementary Materials:** The following are available online at <http://www.mdpi.com/2075-163X/8/8/340/s1>, barioferrite cif files for 100 K, 200 K, 300 K, and 400 K.

**Author Contributions:** A.K. and T.L.P. wrote the paper. A.K. performed the Raman study and also selected the grains for the structural investigations. A.K., I.O.G., and E.V.G. collected samples for investigation during the field work, performed petrological investigations, and measured the composition of the barioferrite from Har Parsa. T.L.P. performed the SC-XRD investigation, refined the barioferrite structure, and interpreted the structural data.

**Funding:** Grant Preludium of the National Science Centre of Poland No. 2016/21/N/ST10/00463.

**Acknowledgments:** The investigations were partially supported by the National Science Centre of Poland, Grant Preludium No. 2016/21/N/ST10/00463. X-ray diffraction studies were performed at the X-ray Diffraction Centre of Saint Petersburg State University. The authors thank the anonymous reviewers for their careful reviews, which helped to improve a previous version of the manuscript.

**Conflicts of Interest:** The authors declare no conflict of interest.

## References

- Murashko, M.N.; Chukanov, N.V.; Mukhanova, A.A.; Vapnik, E.; Britvin, S.N.; Polekhovskiy, Y.S.; Ivakin, Y.D. Barioferrite  $\text{BaFe}_{12}\text{O}_{19}$ : A new mineral species of the magnetoplumbite group from the Haturim Formation in Israel. *Geol. Ore Depos.* **2011**, *53*, 558–563. [CrossRef]
- Obradors, X.; Collomb, A.; Pernet, M.; Samaras, D.; Joubert, J.C. X-ray analysis of the structural and dynamic properties of  $\text{BaFe}_{12}\text{O}_{19}$  hexagonal ferrite at room temperature. *J. Solid State Chem.* **1985**, *56*, 171–181. [CrossRef]
- Bertaut, E.F.; Deschamps, A.; Pauthenet, R. Etude de la substitution de Fe par Al, Ga et Cr dans l'hexaferrite de baryum,  $\text{BaO}(\text{Fe}_2\text{O}_3)_6$ . *J. Phys. Radium* **1959**, 404–408. [CrossRef]
- Aleshko-Ozhevskii, O.P.; Faek, M.K.; Yamzin, I.I. A neutron diffraction study of the structure of magnetoplumbite. *Sov. Phys. Crystallogr.* **1969**, *14*, 367–369.
- Vinnik, D.A.; Zhrebtsov, D.A.; Mashkovtseva, L.S.; Nemrava, S.; Perov, N.S.; Semisalova, A.S.; Krivtsov, I.V.; Isaenko, L.I.; Mikhailov, G.G.; Niewa, R. Ti-Substituted  $\text{BaFe}_{12}\text{O}_{19}$  single crystal growth and characterization. *Cryst. Growth Des.* **2014**, *14*, 5834–5839. [CrossRef]
- Lengauer, C.L.; Tillmanns, E.; Hentschel, G. Batiferrite,  $\text{Ba}[\text{Ti}_2\text{Fe}_{10}]\text{O}_{19}$ , a new ferrimagnetic magnetoplumbite-type mineral from the Quaternary volcanic rocks of the western Eifel area, Germany. *Miner. Petrol.* **2001**, *71*, 1–19. [CrossRef]
- Pullar, R.C. Hexagonal ferrites: A review of the synthesis, properties and applications of hexaferrite ceramics. *Prog. Mater. Sci.* **2012**, *57*, 1191–1334. [CrossRef]
- Žáček, V.; Skála, R.; Chlupáčová, M.; Dvořák, Z. Ca–Fe<sup>3+</sup>-rich, Si-undersaturated buchite from Zelenky, North-Bohemian Brown Coal Basin, Czech Republic. *Eur. J. Mineral.* **2005**, *17*, 623–634. [CrossRef]
- Galuskin, E.V.; Gfeller, F.; Galuskina, I.O.; Pakhomova, A.; Armbruster, T.; Vapnik, Y.; Włodyka, R.; Dzierżanowski, P.; Murashko, M. New minerals with a modular structure derived from hatrurite from the pyrometamorphic Hatrurim Complex. Part II. Zadovite,  $\text{BaCa}_6[(\text{SiO}_4)(\text{PO}_4)](\text{PO}_4)_2\text{F}$  and aradite,  $\text{BaCa}_6[(\text{SiO}_4)(\text{VO}_4)](\text{VO}_4)_2\text{F}$ , from paralavas of the Hatrurim Basin, Negev Desert, Israel. *Mineral. Mag.* **2015**, *79*, 1073–1087. [CrossRef]
- Galuskina, I.O.; Galuskin, E.V.; Vapnik, Y.; Prusik, K.; Stasiak, M.; Dzierżanowski, P.; Murashko, M.; Krivovichev, S. Gurimite,  $\text{Ba}_3(\text{VO}_4)_2$  and hexacelsian,  $\text{BaAl}_2\text{Si}_2\text{O}_8$ —Two new minerals from schorlomite-rich paralava of the Hatrurim Complex, Negev Desert, Israel. *Mineral. Mag.* **2017**, *81*, 1009–1019. [CrossRef]
- Galuskina, I.O.; Galuskin, E.V.; Pakhomova, A.S.; Widmer, R.; Armbruster, T.; Krüger, B.; Grew, E.S.; Vapnik, Y.; Dzierżanowski, P.; Murashko, M. Khesinite,  $\text{Ca}_4\text{Mg}_2\text{Fe}^{3+}_{10}\text{O}_4[(\text{Fe}^{3+}_{10}\text{Si}_2)\text{O}_{36}]$ , a new rhönite-group (sapphirine supergroup) mineral from the Negev Desert, Israel—Natural analogue of the SFCA phase. *Eur. J. Mineral.* **2017**, 101–116. [CrossRef]

12. Picard, L. *Geological Research in the Judean Desert*; Goldberg's Press: Jerusalem, Israel, 1931; p. 108.
13. Kolodny, Y.; Gross, S. Thermal metamorphism by combustion of organic matter: Isotopic and petrological evidence. *J. Geol.* **1974**, *82*, 489–506. [[CrossRef](#)]
14. Burg, A.; Starinsky, A.; Bartov, Y.; Kolodny, Y. Geology of the Hatrurim Formation (“Mottled Zone”) in the Hatrurim basin. *Isr. J. Earth Sci.* **1991**, *40*, 107–124.
15. Burg, A.; Kolodny, Y.; Lyakhovskiy, V. Hatrurim-2000: The “Mottled Zone” revisited, forty years later. *Isr. J. Earth Sci.* **2000**, *48*, 209–223.
16. Townes, W.D.; Fang, J.H.; Perrotta, A.J. The crystal structure and refinement of ferrimagnetic barium ferrite,  $\text{BaFe}_{12}\text{O}_{19}$ . *Z. Kristallogr. Cryst. Mater.* **1967**, *125*, 437–449. [[CrossRef](#)]
17. Aminoff, G. Über ein neues oxydisches mineral aus längban. (Magnetoplumbit.). *Geologiska Föreningen i Stockholm Förhandlingar* **1925**, *47*, 283–289. [[CrossRef](#)]
18. Moore, P.B.; Gupta, P.K.S.; Le Page, Y. Magnetoplumbite,  $\text{Pb}^{2+}\text{Fe}^{3+}_{12}\text{O}_{19}$ : Refinement and lone-pair splitting. *Am. Mineral.* **1989**, *74*, 1186–1194.
19. Shen, S.-P.; Chai, Y.-S.; Cong, J.-Z.; Sun, P.-J.; Lu, J.; Yan, L.-Q.; Wang, S.-G.; Sun, Y. Magnetic-ion-induced displacive electric polarization in  $\text{FeO}_5$  bipyramidal units of  $(\text{Ba},\text{Sr})\text{Fe}_{12}\text{O}_{19}$  hexaferrites. *Phys. Rev. B* **2014**, *90*, 180404. [[CrossRef](#)]
20. Bentor, Y.K. *Lexique Stratigraphique International: Asie fascicule 10 c 2 Israel*; Centre National de la Recherche Scientifique: Paris, France, 1960; Volume 3.
21. Gross, S. The mineralogy of the Hatrurim Formation, Israel. *Geol. Surv. Isr. Bull.* **1977**, *70*, 1–80.
22. Vapnik, Y.; Sharygin, V.V.; Sokol, E.V.; Shagam, R. Paralavas in a combustion metamorphic complex: Hatrurim Basin, Israel. In *Geology of Coal Fires: Case Studies from Around the World*; Geological Society of America: Boulder, CO, USA, 2007; Volume 18, pp. 133–153, ISBN 978-0-8137-4118-5.
23. Novikov, I.; Vapnik, Y.; Safonova, I. Mud volcano origin of the Mottled Zone, South Levant. *Geosci. Front.* **2013**, *4*, 597–619. [[CrossRef](#)]
24. Minster, T.; Yoffe, O.; Nathan, Y.; Flexer, A. Geochemistry, mineralogy, and paleoenvironments of deposition of the Oil Shale Member in the Negev. *Isr. J. Earth Sci.* **1997**, *46*, 41–59.
25. Sokol, E.; Novikov, I.; Zateeva, S.; Vapnik, Y.; Shagam, R.; Kozmenko, O. Combustion metamorphism in the Nabi Musa dome: New implications for a mud volcanic origin of the Mottled Zone, Dead Sea area. *Basin Res.* **2010**, *22*, 414–438. [[CrossRef](#)]
26. Sokol, E.V.; Kozmenko, O.A.; Kokh, S.N.; Vapnik, Y. Gas reservoirs in the Dead Sea area: Evidence from chemistry of combustion metamorphic rocks in Nabi Musa fossil mud volcano. *Russ. Geol. Geophys.* **2012**, *3*, 745–762. [[CrossRef](#)]
27. Galuskin, E.V.; Krüger, B.; Galuskina, I.O.; Krüger, H.; Vapnik, Y.; Wojdyla, J.A.; Murashko, M. New mineral with modular structure derived from hatrurite from the pyrometamorphic rocks of the hatrurim complex: Ariegilatite,  $\text{BaCa}_{12}(\text{SiO}_4)_4(\text{PO}_4)_2\text{F}_2\text{O}$ , from Negev desert, Israel. *Minerals* **2018**, *8*, 109. [[CrossRef](#)]
28. Sokol, E.V.; Seryotkin, Y.V.; Kokh, S.N.; Vapnik, Y.; Nigmatulina, E.N.; Goryainov, S.V.; Belogub, E.V.; Sharygin, V.V. Flamite,  $(\text{Ca},\text{Na},\text{K})_2(\text{Si},\text{P})\text{O}_4$ , a new mineral from ultrahightemperature combustion metamorphic rocks, Hatrurim Basin, Negev Desert, Israel. *Mineral. Mag.* **2015**, *79*, 583–596. [[CrossRef](#)]
29. Sharygin, V.V.; Lazic, B.; Armbruster, T.M.; Murashko, M.N.; Wirth, R.; Galuskina, I.O.; Galuskin, E.V.; Vapnik, Y.; Britvin, S.N.; Logvinova, A.M. Shulamitite  $\text{Ca}_3\text{TiFe}^{3+}\text{AlO}_8$ —A new perovskite-related mineral from Hatrurim Basin, Israel. *Eur. J. Mineral.* **2013**, 97–111. [[CrossRef](#)]
30. Galuskin, E.V.; Galuskina, I.O.; Gfeller, F.; Krüger, B.; Kusz, J.; Vapnik, Y.; Dulski, M.; Dzierzanowski, P. Silicocarnotite,  $\text{Ca}_5[(\text{SiO}_4)(\text{PO}_4)](\text{PO}_4)$ , a new “old” mineral from the Negev Desert, Israel, and the ternesite–silicocarnotite solid solution: Indicators of high-temperature alteration of pyrometamorphic rocks of the Hatrurim Complex, Southern Levant. *Eur. J. Mineral.* **2016**, *28*, 105–123. [[CrossRef](#)]
31. Galuskin, E.V.; Gfeller, F.; Galuskina, I.O.; Armbruster, T.; Krzȩtała, A.; Vapnik, Y.; Kusz, J.; Dulski, M.; Gardocki, M.; Gurbanov, A.G.; et al. New minerals with a modular structure derived from hatrurite from the pyrometamorphic rocks. Part III. Gazeevite,  $\text{BaCa}_6(\text{SiO}_4)_2(\text{SO}_4)_2\text{O}$ , from Israel and the Palestine Autonomy, South Levant, and from South Ossetia, Greater Caucasus. *Mineral. Mag.* **2017**, *81*, 499–513. [[CrossRef](#)]
32. Pouchou, J.L.; Pichoir, F. Quantitative Analysis of Homogeneous or Stratified Microvolumes Applying the Model “PAP”. In *Electron Probe Quantitation*; Springer: Boston, MA, USA, 1991; pp. 31–75, ISBN 978-1-4899-2619-7.

33. Britvin, S.N.; Dolivo-Dobrovolsky, D.V.; Krzhizhanovskaya, M.G. Software for processing the X-ray powder diffraction data obtained from the curved image plate detector of Rigaku RAXIS Rapid II diffractometer. *Proc. Russ. Mineral. Soc.* **2017**, *146*, 104–107.
34. Galuskina, I.O.; Vapnik, Y.; Lazic, B.; Armbruster, T.; Murashko, M.; Galuskin, E.V. Harmunite  $\text{CaFe}_2\text{O}_4$ : A new mineral from the Jabel Harmun, West Bank, Palestinian Autonomy, Israel. *Am. Mineral.* **2014**, *99*, 965–975. [[CrossRef](#)]
35. Kreisel, J.; Lucazeau, G.; Vincent, H. Raman Spectra and Vibrational Analysis of  $\text{BaFe}_{12}\text{O}_{19}$  Hexagonal Ferrite. *J. Solid State Chem.* **1998**, *137*, 127–137. [[CrossRef](#)]
36. Kumar, S.; Supriya, S.; Pandey, R.; Pradhan, L.K.; Singh, R.K.; Kar, M. Effect of lattice strain on structural and magnetic properties of Ca substituted barium hexaferrite. *J. Magn. Magn. Mater.* **2018**, *458*, 30–38. [[CrossRef](#)]
37. Kreisel, J.; Lucazeau, G.; Vincent, H. Raman study of substituted barium ferrite single crystals,  $\text{BaFe}_{12-2x}\text{Me}_x\text{Co}_x\text{O}_{19}$  (Me = Ir, Ti). *J. Raman Spectrosc.* **1999**, *30*, 115–120. [[CrossRef](#)]
38. Silva Júnior, F.M.; Paschoal, C.W.A. Spin-phonon coupling in  $\text{BaFe}_{12}\text{O}_{19}$  M-type hexaferrite. *J. Appl. Phys.* **2015**, *116*, 244110. [[CrossRef](#)]
39. Ganapathi, L.; Gopalakrishnan, J.; Rao, C.N.R. Barium hexaferrite (M-phase) exhibiting superstructure. *Mater. Res. Bull.* **1984**, *19*. [[CrossRef](#)]
40. Sheldrick, G.M. A short history of SHELX. *Acta Crystallogr. Sect. Found. Crystallogr.* **2008**, *64*, 112–122. [[CrossRef](#)] [[PubMed](#)]
41. Agilent Technologies. *CrysAlisCCD and CrysAlis Red*; Oxford Diffraction Ltd.: Oxford, UK, 2014.
42. Momma, K.; Izumi, F. VESTA 3 for three-dimensional visualization of crystal, volumetric and morphology data. *J. Appl. Crystallogr.* **2011**, *44*, 1272–1276. [[CrossRef](#)]
43. Nagashima, M.; Armbruster, T.; Hainschwang, T. A temperature-dependent structure study of gem-quality hibonite from Myanmar. *Mineral. Mag.* **2010**, *74*, 871–885. [[CrossRef](#)]
44. Siegrist, T.; Vanderah, T.A. Combining magnets and dielectrics: Crystal chemistry in the  $\text{BaO-Fe}_2\text{O}_3\text{-TiO}_2$  System. *Eur. J. Inorg. Chem.* **2003**, 1483–1501. [[CrossRef](#)]
45. Shannon, R.D. Revised effective ionic radii and systematic studies of interatomic distances in halides and chalcogenides. *Acta Crystallogr. Sect. Cryst. Phys. Diffr. Theor. Gen. Crystallogr.* **1976**, *32*, 751–767. [[CrossRef](#)]
46. An, S.Y.; Shim, I.-B.; Kim, C.S. Mössbauer and magnetic properties of Co-Ti substituted barium hexaferrite nanoparticles. *J. Appl. Phys.* **2002**, *91*, 8465–8467. [[CrossRef](#)]
47. Hofmeister, A.M.; Wopenka, B.; Locock, A.J. Spectroscopy and structure of hibonite, grossite, and  $\text{CaAl}_2\text{O}_4$ : Implications for astronomical environments. *Geochim. Cosmochim. Acta* **2004**, *68*, 4485–4503. [[CrossRef](#)]
48. Bermanec, V.; Holtstam, D.; Sturman, D.; Criddle, A.J.; Back, M.E.; Scavnicar, S. Nezilovite, a new member of the magnetoplumbite group, and the crystal chemistry of magnetoplumbite and hibonite. *Can. Mineral.* **1996**, *34*, 1287–1297.
49. Ardit, M.; Borcănescu, S.; Cruciani, G.; Dondi, M.; Lazău, I.; Păcurariu, C.; Zanelli, C. Ni-Ti codoped hibonite ceramic pigments by combustion synthesis: Crystal structure and optical properties. *J. Am. Ceram. Soc.* **2016**, *99*, 1749–1760. [[CrossRef](#)]
50. Giannini, M.; Ballaran, T.B.; Langenhorst, F. Crystal chemistry of synthetic Ti–Mg-bearing hibonites: A single-crystal X-ray study. *Am. Mineral.* **2014**, *99*, 2060–2067. [[CrossRef](#)]
51. Kitagawa, Y.; Hiraoka, Y.; Honda, T.; Ishikura, T.; Nakamura, H.; Kimura, T. Low-field magnetoelectric effect at room temperature. *Nat. Mater.* **2010**, *9*, 797–802. [[CrossRef](#)] [[PubMed](#)]
52. Graetsch, H.; Gebert, W. Positional and thermal disorder in the trigonal bipyramid of magnetoplumbite structure type  $\text{SrGa}_{12}\text{O}_{19}$ . *Z. Kristallogr.* **1994**, *209*, 338–342. [[CrossRef](#)]
53. Galuskin, E.V.; Galuskina, I.O.; Widmer, R.; Armbruster, T. First natural hexaferrite with mixed  $\beta'''$ -ferrite ( $\beta$ -alumina) and magnetoplumbite structure from Jabel Harmun, Palestinian Autonomy. *Eur. J. Mineral.* **2018**. [[CrossRef](#)]

